ELSEVIER

Computers & Geosciences 33 (2007) 1064–1075

COMPUTERS & GEOSCIENCES

www.elsevier.com/locate/cageo

Algorithms for the calculation of exact displacements, strains, and stresses for triangular dislocation elements in a uniform elastic half space ☆

Brendan J. Meade*

Department of Earth and Planetary Sciences, Harvard University, 20 Oxford St., Cambridge, MA 02138, USA

Received 5 August 2006; received in revised form 6 December 2006; accepted 10 December 2006

Abstract

We present algorithms for analytically calculating the displacements, strains, and stresses associated with slip on a triangular dislocation element (TDE) in a homogeneous elastic half space. Following previous efforts, the solution is constructed as a dislocation loop where the deformation fields for each of the three triangle legs are calculated by the superposition of two angular dislocations. In addition to the displacements at the surface we derive the displacements and strains at arbitrary depth. We give explicit formulas for the strains due to slip on an angular dislocation, the calculation of angular dislocation slip components, a method for identifying observation coordinates affected by a solid body translation, and rules for internally consistent vertex ordering allowing for the superposition of multiple TDEs. Examples of surface displacements and internal stresses are given and compared with rectangular representations of geometrically complex fault surfaces.

Keywords: Elastic dislocation; Faulting; Seismotectonics

1. Introduction

Elastic dislocation theory is widely used for calculating the displacements, strains, and stresses associated with faulting from earthquake rupture to interseismic time scales (e.g., Burgmann et al., 2002; McGuire and Segall, 2003; Savage and Burford, 1973). Fault surfaces are often parameterized as a collection of point or rectangular sources due to the availability of analytic solutions for the deformation due to slip on dislocation elements of these shapes (e.g., Okada, 1985, 1992). However, some faults, such as those at subduction zones, may have geometries with substantial variations in both strike and dip. Rectangular parameterizations of complex fault surfaces exhibit geometric gaps due to the fact that it is often impossible to mesh non-planar surfaces exactly using rectangular elements. The effect of these gaps is to complicate the accurate calculation of displacements and stresses due to the effects of strain singularities at the edge of every dislocation element. These effects vanish, except exactly at element edges, with gap-free parameterizations of fault surfaces. With gap-free representations of fault surfaces these effects vanish

☆ Code available from server at http://www.iamg.org/CGEditor/index.htm

*Tel.: +1 617 495 8921; fax: +1 617 495 8839.
E-mail address: meade@fas.harvard.edu.

0098-3004/$ - see front matter © 2007 Elsevier Ltd. All rights reserved.
doi:10.1016/j.cageo.2006.12.003

everywhere, except along dislocation edges, because each singular boundary is matched exactly with another. Gap-free tessellation of observationally constrained fault surface geometry can be achieved using triangular meshes (e.g., Plesch et al., 2003) and we develop a solution for the static elastic response to slip on an arbitrary set of triangular dislocation elements (TDEs). These algorithms facilitate the accurate modeling of geometrically complex of fault zones and may be useful for Coulomb failure stress calculations, modeling geodetic measurements, quasi-dynamic rupture simulations, and the assessment of the geometric continuity of active faults.

The concept of a TDE in a homogeneous elastic half space is not a new one. Several studies over the last 30 years have contributed to the development of the techniques that might be used to construct TDEs from primitive Green's functions. Brown (1975) discussed the superposition of angular dislocations to construct the sides of a polygon. This construction was enabled by the calculation of Green's functions for an angular dislocation in a uniform elastic half space given by Comninou (1973) and Comninou and Dunders (1975). Both Comninou (1973) and Jeyakumaran et al. (1992) outlined the rotation and translation needed to map an arbitrary dislocation leg into the angular dislocation coordinate system formalized by Comninou and Dunders (1975). Thomas (1993) extended Jeyakumaran et al.'s (1992) boundary element formulation to arbitrary polygonal dislocation elements and noted typographical errors in the formulas for the displacements due to slip on an angular dislocation (Comninou and Dunders, 1975). These algorithms have been used to study fault interactions (Griffith and Cooke, 2004; Olson and Cooke, 2005) and as the basis for the inversion of geodetic measurements for coseismic slip distributions (Maerten et al., 2005). Despite these contributions the application of TDEs has not been widespread due to the fact that their construction has remained opaque.

Here, we present explicit algorithms to analytically calculate the displacements and strains associated with slip on a TDE beginning with a review of the construction of a dislocation loop by means of the superposition of angular dislocations. We detail the geometric transformations necessary to calculate the angular dislocation geometries from the triangle vertices, and project the triangular element slip vector into the slip vectors for each angular dislocation element. Exact expressions for the strains due to an angular dislocation in an elastic half space are presented (Appendix A). The strains and stresses at depth for a TDE are given by the rotation and superposition of strains from each angular dislocation. We develop an algorithm for identifying observation coordinates below the surface of a TDE affected by a solid body offset. The deformation fields associated with multiple TDEs are readily constructed by superposition using a vertex ordering scheme that is consistent from element to element. Comparisons between the displacement and stress fields for triangular and rectangular representations of non-planar fault surfaces demonstrate the effects of alternate geometric parameterizations of fault surfaces.

2. Construction of TDEs

To calculate the displacements, $\mathbf{u}$, at a point $\mathbf{r}$, due to slip, b_i, on a dislocation element with a surface S, we can integrate the product of the displacement discontinuity and the stress produced at a point, $\mathbf{r}'$, over the surface

$$\mathbf{u}(\mathbf{r}) = \int_S b_i C_{ijkl} n_j \partial_l \mathbf{u}_k(\mathbf{r}' - \mathbf{r})\, \mathrm{d}S, \tag{1}$$

where n_j is a unit vector in the j direction, b_i is the slip vector in the i direction, and u_{mk} is the tensor Green's function for the elastic displacements (e.g., Hirth and Lothe, 1968). Assuming a homogeneous elastic body with Lamé parameters, μ and λ, the elastic moduli tensor can be written as $C_{ijkl} = \mu(\delta_{ik}\delta_{jl} + \delta_{il}\delta_{jk}) + \lambda\delta_{ij}\delta_{kl}$ (δ_{ij} is Kronecker's delta) (e.g., Malvern, 1969) and, along with Stokes theorem, Burgers (1939) demonstrated that (1) can be rewritten in terms of contour integrals as

$$\mathbf{u}(\mathbf{r}) = \frac{\mathbf{b}\Omega}{4\pi} + \frac{1}{4\pi}\oint_C \frac{\mathbf{b}\times\mathbf{n}_l}{||\mathbf{r}' - \mathbf{r}||}\,\mathrm{d}l + \frac{1}{4\pi(1-\nu)}\nabla\oint_C \frac{(\mathbf{b}\times(\mathbf{r}' - \mathbf{r}))\cdot\mathbf{n}_l}{||\mathbf{r}' - \mathbf{r}||}\,\mathrm{d}l, \tag{2}$$

where $\nu = \mu/2(\lambda+\mu)$ is Poisson's ratio. The first term in Eq. (2) gives the displacement discontinuity (solid angle offset) across the surface of the dislocation element, while the second and third terms are continuous and give the elastic effects as line integrals around the boundary of the dislocation surface serving as the foundation for the concept of a dislocation loop (e.g., Hirth and Lothe,

1968). Thus, to calculate the total deformation associated with uniform slip on a single TDE we can calculate the appropriate line integrals around the element edges (legs) so that the total displacement is given by the sum of the displacements from each of the three legs (Fig. 1). The basic concept is to use angular dislocations to construct a solid prism, with the TDE defining its top surface, which is displaced in the same direction as the TDE slip vector (Fig. 1). Internally consistent vertex ordering causes the elastic effects due to prism edges below the TDE surface to vanish leaving only the elastic effects associated with the boundary of the TDE. This approach is identical to that outlined in previous studies of the construction of TDEs (Brown, 1975; Comninou, 1973; Jeyakumaran et al., 1992; Thomas, 1993).

A TDE is geometrically defined by three vertices ($\mathbf{p}_1$,$\mathbf{p}_2$,$\mathbf{p}_3$) (Fig. 1) and for the purpose of this application we define a vertex ordering system that ensures that the vertical legs of the angular dislocation elements cancel exactly. The vertex ordering scheme we use here enforces a clockwise sense of circulation for triangle vertices when viewed from above (Fig. 2). Triangle vertices are defined as having a clockwise orientation if the z component of the unit vector normal to the triangle face is positive, $((\mathbf{p}_2-\mathbf{p}_1)\times(\mathbf{p}_3-\mathbf{p}_1))_z>0$. If this quantity is negative then any two triangle vertices can be swapped and the triangle normal vector will then be positive. With the vertices for all triangles ordered in a clockwise fashion the sense of slip and orientation of the unit vectors will be consistent

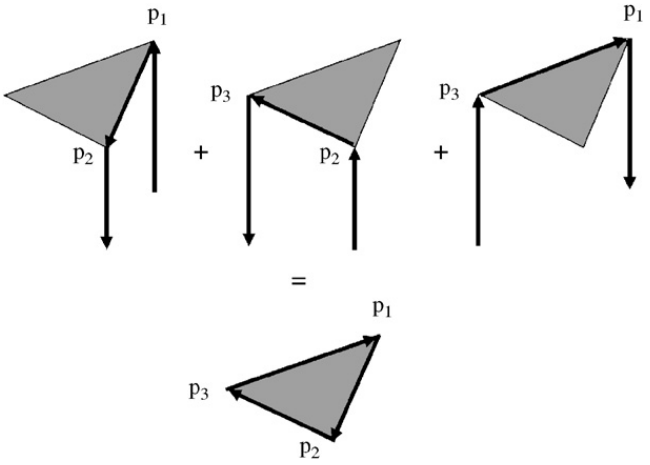

Fig. 1. Triangular dislocation element and triangle leg geometry. Arrows indicate sense of orientation of the slip components. Note that vertical segments of each dislocation leg cancel exactly with those of adjacent legs.

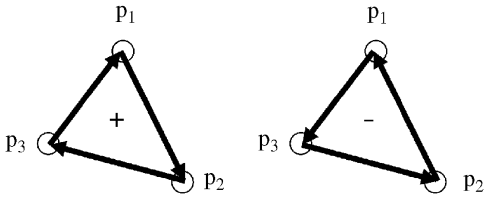

Fig. 2. Vertex ordering. (a) Clockwise vertex ordering where the unit vector normal to the face has a positive (+) z component. (b) Counter-clockwise vertex ordering where the unit vector normal to the face has a negative (−) z-component.

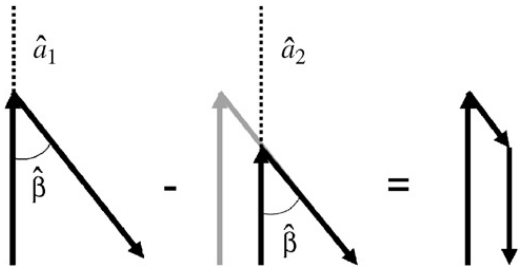

Fig. 3. Construction of a single dislocation leg by means of summation of two angular dislocations. Inclination of each angular dislocation is given by a common inclination $\hat{\beta}$ while vertices are buried to depths $\hat{a}_1$ and $\hat{a}_2$ respectively. Common, dipping segment of each angular dislocation cancels after summation.

from one element to the next regardless of its orientation. Using this vertex ordering system it is straightforward to construct consistent representations of geometrically complex surfaces using TDEs by superposition of individual elements.

The total deformation field for a TDE can be calculated by summing the deformation fields from each of the dislocation legs that defines the boundary of the element. Each of the three legs can be constructed by the superposition of two angular dislocations between each set of triangle vertices (Fig. 3). We calculate the displacement from each leg, $\mathbf{u}_k$, by the superposition of deformation fields from two angular dislocations (i.e., $\mathbf{u}_k = \mathbf{u}_k^{(1)} - \mathbf{u}_k^{(2)}$):

$$\mathbf{u} = \sum_{j=1}^{N}\sum_{k=1}^{3} \mathbf{u}_{k_j}^{(1)} - \mathbf{u}_{k_j}^{(2)}, \tag{3}$$

where k and j are indices over the three legs of each triangle and each TDE respectively, and N is the number of TDEs (Comninou, 1973; Jeyakumaran et al., 1992). In constructing TDEs from angular dislocation legs there are two major tasks to enable the summation in Eq. (3). The first is the calculation of the angular dislocation geometry in terms of the

TDE vertices and the second is the calculation of the appropriate slip vectors on each angular dislocation. The displacements scale linearly with the magnitude of slip.

Green's functions for the surface and internal displacements due to slip on a buried angular dislocation, $\mathbf{u}_k$ in Eq. (3), are known for both a whole space (Yoffe, 1960) and, most relevant to geophysical applications, a half space (Comninou, 1973; Comninou and Dunders, 1975). These studies give exact expressions (not repeated here) for the surface and internal displacements due to strike-, dip-, and tensile-slip on a buried angular dislocation in the $x-z$ plane with a vertex located at the origin in the $x-y$ plane. The geometry of an angular dislocation is defined by an area of uniform slip along a vertical surface in the plane bounded by two semi-infinite line segments which meet at a point below the free surface at a depth, $\hat{a}$, where the caret denotes the variable's association with a particular angular dislocation. The geometry of an angular dislocation is further defined by the inclination, $\hat{\beta}$, which can be written in terms of the leg dip, $\hat{\delta}$, as

$$\hat{\beta} = \begin{cases} \pi/2 - \hat{\delta} & \text{if } \hat{\delta} \geqslant 0, \\ -\pi/2 - \hat{\delta} & \text{if } \hat{\delta} < 0, \end{cases} \tag{4}$$

where the leg dip is given by $\tan\hat{\delta} = \Delta p_z/(\Delta p_x \cos\hat{\alpha} + \Delta p_y \sin\hat{\alpha})$. Note that the difference in position, $\Delta\mathbf{p} = \mathbf{p}_{i+1} - \mathbf{p}_i$, of the leg endpoints (two TDE vertices) depends on the vertex ordering. Additionally, to maintain a consistent sense of the orientation for the vertical segment of each angular dislocation we ensure that $0 \leqslant \hat{\beta} \leqslant \pi/2$. If the first angular dislocation lies in the $x-z$ plane with a vertex at a depth $\hat{\alpha}$ and is inclined at an angle $\hat{\beta}$ (inclination) a second dislocation element with a vertex along the non-vertical line segment (at a depth of $\hat{\alpha}$) and slip opposite to that of the first angular dislocation will cancel all deformation except that due to the polygonal slip patch below the leg of the triangular element (Fig. 3). Note that there is no deformation for the $\hat{\beta} = 0$ case.

Transforming the TDE vertices to the Comninou and Dunders (1975) coordinate system for each of the angular dislocations requires that the coordinates for each leg are mapped as $(\mathbf{p}_1, \mathbf{p}_2) \rightarrow (\hat{\mathbf{p}}_1, \hat{\mathbf{p}}_2)$, $(\mathbf{p}_2, \mathbf{p}_3) \rightarrow (\hat{\mathbf{p}}_1, \hat{\mathbf{p}}_2)$, $(\mathbf{p}_3, \mathbf{p}_1) \rightarrow (\hat{\mathbf{p}}_1, \hat{\mathbf{p}}_2)$ where the depth, a, to each vertex is defined as positive and the coordinates $(\hat{\mathbf{p}}_1, \hat{\mathbf{p}}_2)$ define the rotated leg endpoints for each of the TDE legs. The transform between the two coordinate systems is given by a rotation of coordinates, $\hat{\mathbf{p}} = \boldsymbol{\omega}\mathbf{p}$, where the rotation matrix, $\boldsymbol{\omega}$, is a function of the strike, $\tan\hat{\alpha} = \Delta y/\Delta x$, of each dislocation leg,

$$\boldsymbol{\omega} = \begin{pmatrix} \cos\hat{\alpha} & \sin\hat{\alpha} & 0 \\ -\sin\hat{\alpha} & \cos\hat{\alpha} & 0 \\ 0 & 0 & 1 \end{pmatrix}. \tag{5}$$

The observation coordinates can also be translated and rotated into the Comninou and Dunders (1975) coordinate system so that each angular dislocation lies in the $\hat{x} - \hat{z}$ plane.

$$\hat{s} = \boldsymbol{\omega}(\mathbf{s} - \mathbf{p}) \tag{6}$$

Using these relations and Green's functions from Comninou and Dunders (1975) we can calculate both the internal and surface displacement fields for an angular dislocation. As an example, consider the angular dislocation shown in Fig. 4 with a vertex at $(x = -25, y = 0, z = \hat{a} = 0)$ aligned along the x-axis $(\hat{\alpha} = 0)$ and dipping at 45° so that $\hat{\beta} = 45°$ with unit strike-slip motion. The internal displacements are shown in the $x-y$ plane (Figs. 4a, d). Note the relatively uniform slip over the dislocation surface that is parallel to the strike of the dislocation element and not a function of its inclination, $\hat{\beta}$. Observation coordinates are offset slightly in the positive y direction to highlight the elastic effects. This gives rise to non-zero displacements outside of the angular dislocation patch because the observation coordinates are not coincident with the $x-z$ nodal plane. The surface displacements show the basic four-quadrant pattern of deformation associated with right-lateral strike-slip motion on a vertical dislocation (Fig. 4d). A second angular dislocation in the same plane and with the same inclination as the previous one can be defined with a vertex at $(x = 25, y = 0, z = \hat{a} = 50)$. With unit right-lateral strike-slip the displacements are clearly related to the faulting mechanism in the cross-sectional view (Fig. 4b), while the surface displacements show a rather more diffuse pattern of deformation due to the fact that the angular dislocation source is buried (Fig. 4e). The difference between the displacement fields from these two angular dislocations gives the displacements associated with a dislocation leg, $\mathbf{u}_l = \mathbf{u}^{(1)} - \mathbf{u}^{(2)}$, between the two vertices. The cross-sectional view (Fig. 4c) shows resulting dislocation surface and that the displacements between nearly vanish outside of the boundary of these two surfaces

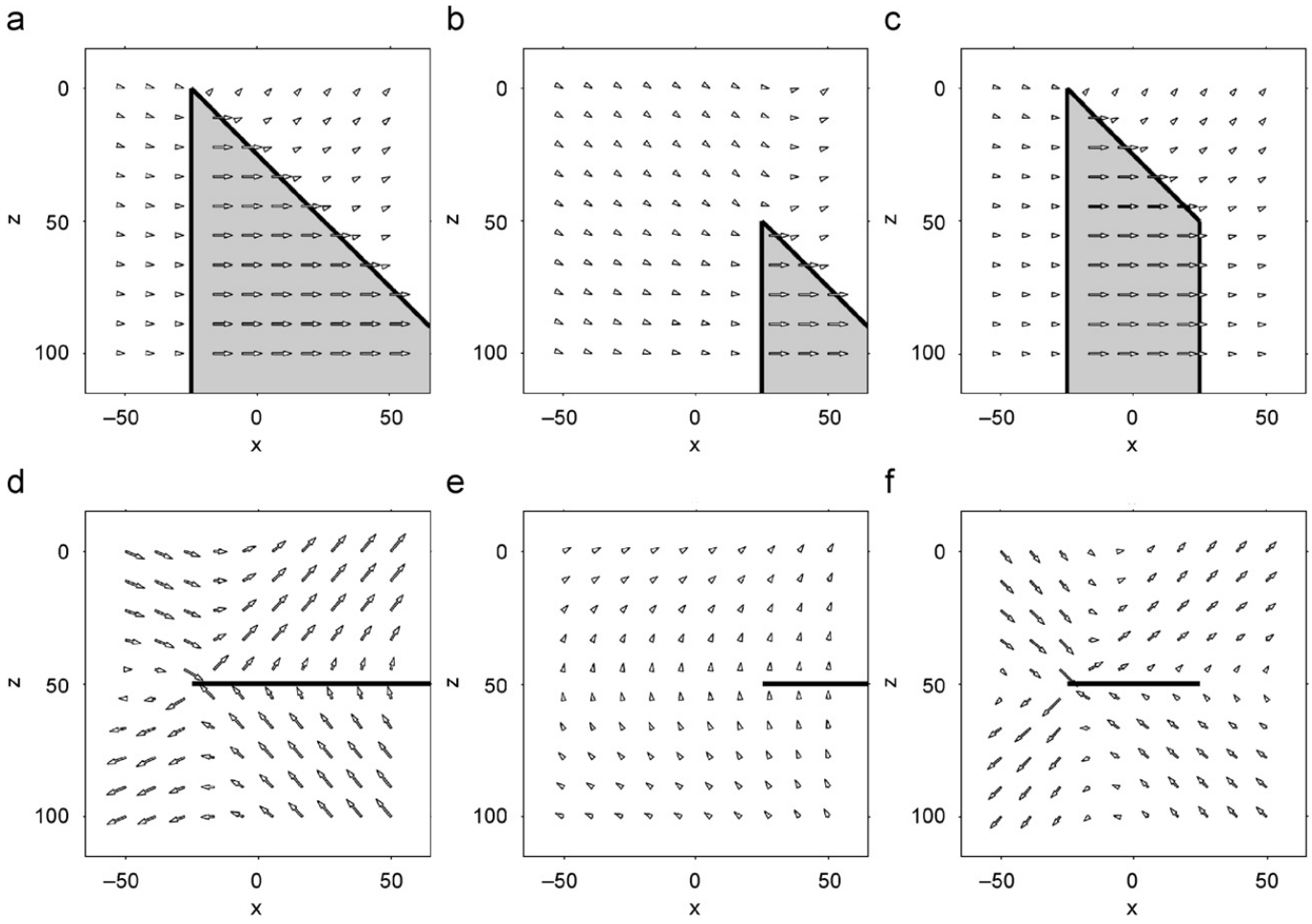

Fig. 4. Displacement fields for strike-slip motion on angular dislocations. (a) Cross-sectional view of displacement for an angular dislocation with a vertex at zero depth and an inclination of 45°. Displacements are non-zero off of the displacement surface due to the fact that observation plane has been offset slightly from nodal plane along $y = 0$ to highlight elastic effects. (b) Same as (a) only for a dislocation with a vertex at a depth of 50 and offset in the positive y direction by 50 units. Thus dipping segment of angular dislocation aligns with that from (a). (c) Displacements from dislocation leg calculated by subtracting (b) from (a). (d–f) Surface displacement fields corresponding to dislocations shown in panels (a–c).

four-quadrant pattern of deformation results at the surface (Fig. 4f).

3. Slip components on the angular dislocations

To calculate the deformation associated with generalized slip in an arbitrary direction on a TDE we must convert the TDE Burgers vector into strike-, dip-, and tensile-slip components on each angular dislocation. Comninou (1973) and Jeyakumaran et al. (1992) outlined a method based on the construction of rotation matrices as functions of unspecified angles. We construct our solution by relating the geometry of the TDE to that of each angular dislocation using orthogonal unit vectors to describe their respective orientations, and projecting the slip vectors from the TDE on to each angular dislocation patch. Using this method with the vertex ordering scheme described above ensures that coordinate transforms are consistent from leg to leg and triangle to triangle.

Given component tensile-, strike-, and dip-slip components of slip, $\mathbf{s}$, on a triangular fault patch we would like relate these to a total slip vector, $\mathbf{v}_s$. We do this by first projecting the Burgers vector into x,y,z coordinates by defining unit vectors normal to the TDE face, one parallel to the direction of strike and one down-dip. A unit vector normal to the face of the triangle is given by, $\mathbf{n}_t = (\mathbf{p}_1 \times \mathbf{p}_2)/||(\mathbf{p}_1 \times \mathbf{p}_2)||$, while one parallel to the strike of the patch is $\mathbf{n}_s = (-\sin\gamma, \cos\gamma, 0)$, where $\gamma = \tan^{-1}(n_t^{(y)}/n_t^{(x)})$. A third direction vector can be defined parallel to the TDE dip as, $\mathbf{n}_d = \mathbf{n}_t \times \mathbf{n}_s$. The fault slip vector is then calculated by dotting the slip components

into each unit vector:

$$\mathbf{v}_s = \begin{pmatrix} v_s^{(x)} \\ v_s^{(y)} \\ v_s^{(z)} \end{pmatrix} = \begin{pmatrix} n_t^{(x)} & n_s^{(x)} & n_d^{(x)} \\ n_t^{(y)} & n_s^{(y)} & n_d^{(y)} \\ n_t^{(z)} & n_s^{(z)} & n_d^{(z)} \end{pmatrix} \begin{pmatrix} s_t \\ s_s \\ s_d \end{pmatrix}. \quad (7)$$

Note that neither $\mathbf{v}_s$ nor the slip components on each triangular patch are, in general, not the same as the slip components on any angular dislocation. The slip vector must be projected into strike-, dip-, and tensile-slip components for each of the three different dislocation legs. To do this we first find the orientation of unit normal vectors in the direction of each component of slip on each angular dislocation. The strike- and tensile-slip components are parallel and perpendicular to the strike of the dislocation leg $\hat{\mathbf{n}}_s = (\cos(\alpha), \sin(\alpha), 0)$, $\hat{\mathbf{n}}_t = (-\sin(\alpha), \cos(\alpha), 0)$, respectively, while the dip-slip unit vector is orthogonal to the plane defined by these two vectors, $\hat{\mathbf{n}}_d = \hat{\mathbf{n}}_s \times \hat{\mathbf{n}}_t$. Due to the fact that $\hat{\mathbf{n}}_s$ and $\hat{\mathbf{n}}_t$ always lie in the $\hat{x} - \hat{y}$ plane the unit vector in the direction of the dip-slip on an angular dislocation is always vertical, $\hat{\mathbf{n}}_d = \mathbf{n}^{(z)} = (0, 0, 1)$. For each angular dislocation we must resolve the slip vector into the corresponding strike-, dip-, and tensile-slip components.

$$\hat{\mathbf{s}} = \begin{pmatrix} \hat{s}_t \\ \hat{s}_s \\ \hat{s}_d \end{pmatrix} = \begin{pmatrix} \hat{n}_t^{(x)} & \hat{n}_s^{(x)} & \hat{n}_d^{(x)} \\ \hat{n}_t^{(y)} & \hat{n}_s^{(y)} & \hat{n}_d^{(y)} \\ \hat{n}_t^{(z)} & \hat{n}_s^{(z)} & \hat{n}_d^{(z)} \end{pmatrix} \begin{pmatrix} v_s^{(x)} \\ v_s^{(y)} \\ v_s^{(z)} \end{pmatrix}, \quad (8)$$

where the subscripts t, s, and d refer to the tensile-, strike-, and dip-slip components, respectively. The projection of the slip vector, $\mathbf{v}_s$, to slip components on an angular dislocation depends only on the strike of the angular dislocation, $\hat{\alpha}$, not on inclination of the angular dislocation, $\hat{\beta}$. While the slip components on each angular dislocation are not a function of the inclination, the displacements from each leg are. With the slip components known for each angular dislocation element we can calculate $\hat{\mathbf{u}}^{(1)}$ and $\hat{\mathbf{u}}^{(2)}$ for each angular dislocation. These displacement fields can then be rotated, $\mathbf{u}^{(i)} = \boldsymbol{\omega}^{-1}\hat{\mathbf{u}}^{(i)}$, and summed, as shown in Eq. (3), to give the total displacement, $\mathbf{u}$, associated with slip on a TDE.

The surface displacements for three legs of a dipping TDE with a uniform strike-slip displacement discontinuity and the total displacement field show how the deformation from individual legs sum to give the total displacement field (Fig. 5). Vertex coordinates, inclination angles, normal vectors and slip components are given in Table 1. For the leg parallel to the direction of TDE slip (Fig. 5a) the angular dislocation slip components are strike-slip only while they are tensile-slip only for the leg oriented perpendicular to the slip direction (Fig. 5c) and mixed for the obliquely oriented leg (Fig. 5b). Note that while slip on individual TDE legs may yield symmetric displacements (Fig. 5a) the overall effect of TDE dip is to generate an asymmetric displacement field where displacements are larger on the hanging wall side (Fig. 5d) due the effects of the dipping legs (Figs. 5b, c).

4. Displacements at depth

The solution by summation of angular dislocations involves the displacement of the entire prism below the TDE in the direction of the displacement vector. By summing the angular dislocations the elastic effects of down-going dislocation segments cancel and we are left with only the elastic effects associated with the triangular element. However, the displacements directly below the TDE see contributions from not only the elastic effects of the TDE but also from the translation of the entire prism. This effect can be modeled by subtracting the displacement vector for observation points below the TDE.

For those observation points whose x–y coordinates lie within the projection of the TDE into the x–y plane we can determine which are below the TDE. If a line segment between the observation coordinates, $\mathbf{s}$, and a point sharing the same x,y coordinates at the free surface intersects with the plane defined by the vertices of the TDE then the equations for the two will be equivalent at the point of intersection. Using a parametric representation of both the plane and line segment we can solve for a single parameter, τ, whose sign determines whether or not the observation point is below the TDE:

$$\tau = \det\begin{vmatrix} 1 & 1 & 1 & 1 \\ p_1^{(x)} & p_2^{(x)} & p_3^{(x)} & s^{(x)} \\ p_1^{(y)} & p_2^{(y)} & p_3^{(y)} & s^{(y)} \\ p_1^{(z)} & p_2^{(z)} & p_3^{(z)} & s^{(z)} \end{vmatrix} \div \det\begin{vmatrix} 1 & 1 & 1 & 0 \\ p_1^{(x)} & p_2^{(x)} & p_3^{(x)} & 0 \\ p_1^{(y)} & p_2^{(y)} & p_3^{(y)} & 0 \\ p_1^{(z)} & p_2^{(z)} & p_3^{(z)} & s^{(z)} \end{vmatrix}, \quad (9)$$

where ($\mathbf{p}_1$,$\mathbf{p}_2$,$\mathbf{p}_3$) are the triangle vertices and $\mathbf{s}$ are the observation coordinates (e.g., Tremblay, 2004). For observation points that are located within the prism and below the TDE the total displacement

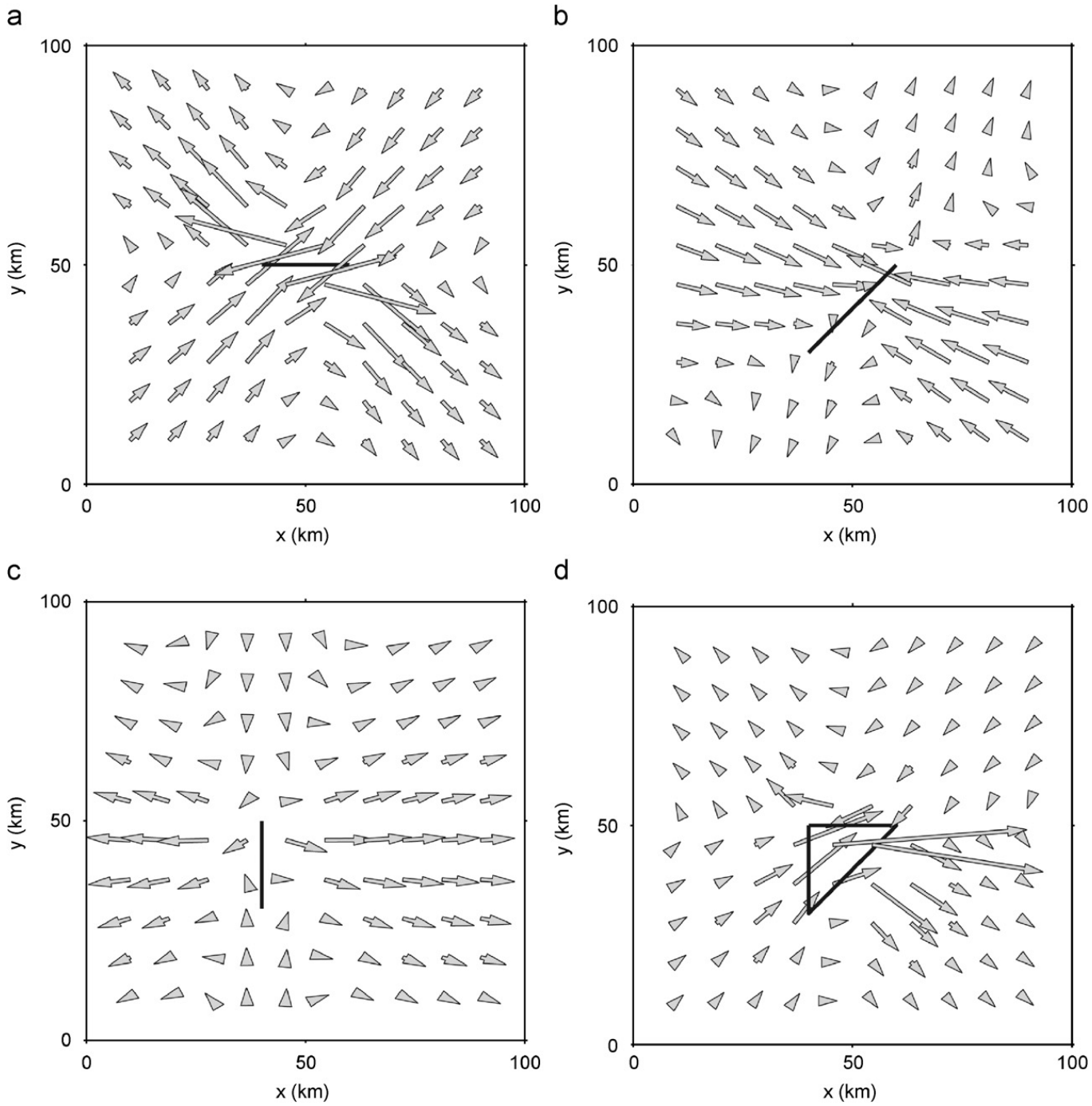

Fig. 5. Surface displacement fields for individual dislocation legs and a complete triangular dislocation element. (a–c) Surface displacement fields for three dislocation legs described in Table 1. (d) Total displacement field resulting from summation of displacement fields from all three legs (a–c). Note that near-fault displacements are larger in hanging wall side than footwall side.

vector can be calculated by subtracting the slip vector $\mathbf{v}_s$:

$$\mathbf{u} = \begin{cases} \mathbf{u} & \text{if } \tau > 0, \\ \mathbf{u} - \mathbf{v}_s & \text{if } \tau < 0 \end{cases} \tag{10}$$

assuming that the depth of the observation coordinate, $s^{(z)}$, is always positive. This correction does not eliminate the singularities along the edges of all angular dislocations which preclude displacement calculations directly below any TDE vertex.

5. Strains and stresses for a TDE

Similar to the displacements, the strains and stresses associated with a TDE can be calculated by

Table 1
Parameters for a simple triangular dislocation element

Quantity	Leg 1	Leg 2	Leg 3
$\mathbf{p}_1$	(40,50,0)	(60,50,0)	(40,30,20)
$\mathbf{p}_2$	(60,50,0)	(40,30,20)	(40,50,0)
$\hat{\beta}$	90	$-\tan^{-1}\sqrt{2}$	45
$\hat{\alpha}$	180	45	−90
$\hat{\mathbf{n}}_s$	(−1,0,0)	$(\sqrt{2}/2, \sqrt{2}/2, 0)$	(0,−1,0)
$\hat{\mathbf{n}}_d$	(0,0,1)	(0,0,1)	(0,0,1)
$\hat{\mathbf{n}}_t$	(0,−1,0)	$(-\sqrt{2}/2, \sqrt{2}/2, 0)$	(1,0,0)
$\hat{s}_s$	−1	$\sqrt{2}/2$	0
$\hat{s}_d$	0	0	0
$\hat{s}_t$	0	$-\sqrt{2}/2$	1

summing the stresses from six separate angular dislocations. The expressions for the stresses from an angular dislocation in an elastic half space can be derived by differentiating Green's functions given by Comninou and Dunders (1975) and applying the definition of strain, $\boldsymbol{\varepsilon} = \frac{1}{2}(\nabla\mathbf{u} + (\nabla\mathbf{u})^{\mathrm{T}})$, where $\nabla\mathbf{u}$ is the deformation gradient tensor. The derivatives of the displacements are somewhat lengthy and were calculated with symbolic algebra computer software in an effort to avoid human error (see Appendix A). The strains from each dislocation leg, $\boldsymbol{\varepsilon}_l = \boldsymbol{\varepsilon}^{(1)} - \boldsymbol{\varepsilon}^{(2)}$, must be rotated about the z-axis and summed get total strain tensor:

$$\boldsymbol{\varepsilon} = \sum_{k=1}^{3} \boldsymbol{\omega}_k^{-1}(\boldsymbol{\varepsilon}_k^{(1)} - \boldsymbol{\varepsilon}_k^{(2)})\boldsymbol{\omega}_k, \tag{11}$$

where the rotation matrix is given by Eq. (5). Once the strains have been summed the stresses can be calculated using Hooke's law for a linear elastic solid, $\sigma = \lambda\,\mathrm{tr}(\boldsymbol{\varepsilon})\mathbf{I} + 2\mu\boldsymbol{\varepsilon}$, where $\mathrm{tr}(\boldsymbol{\varepsilon})$ is the trace of the strain tensor and $\mathbf{I}$ is the identity matrix. Analytic expressions for the strains are somewhat lengthy and are given in Appendix A of supplementary data (see Appendix A). In addition, MATLAB implementations of the complete set of algorithms for both the displacements and strains are given in Appendix B of supplementary data (see Appendix A).

6. Examples of displacement and stress fields

A few simple comparisons can be made between the well-known solutions for the deformation fields surrounding a rectangular dislocation element (e.g., Okada, 1985) and those from two TDEs combined to form a rectangular dislocation element (Fig. 6). Upon summation the common diagonal legs, l_c, from each triangle cancel leaving only the contributions from the perimeter legs (l_1, l_2, l_3, l_4). If we construct a rectangular dislocation element from two TDEs and compare the surface displacements for unit strike-slip on a vertical fault 20 km^2, the two displacement fields agree to one part in 10^{15} which is on the order of double precision for values near unity. This is in agreement with Jeyakumaran et al.'s (1992) finding that the case of two vertical TDEs (used to form a composite rectangle) yield a solution that is algebraically identical to that presented by Chinnery (1961) for a vertical strike-slip fault.

A second reference case is that developed by Thomas' (1993) consisting of a unit dip-slip on a single 2×2 km rectangular dislocation element buried with its centroid at a depth of 2 km and inclined at 45°. Similar to the construction shown in Fig. 6 we can also calculate the deformation associated with slip on this same dislocation patch by the superposition of two TDEs which divide the reference rectangle into two across a diagonal of length $4/\sqrt{2}$ km. For this problem we find that the difference between surface displacement fields from the rectangular solution (e.g., Okada, 1985) and the TDE solution presented here differs by a maximum of one part in 10^{15} while Thomas (1993) reported a agreement at the level of one part in 10^4. Jeyakumaran et al. (1992) give a maximum discrepancy of one part in 10^3 for an unspecified dipping fault model.

Thus far we have considered TDEs dominated by right and 45° angles. The displacements and stresses resulting from slip on an obliquely oriented, dipping and partially buried TDE highlight the generality of the algorithms presented above and the complexity of the resulting deformation fields. Consider a TDE with vertices located at

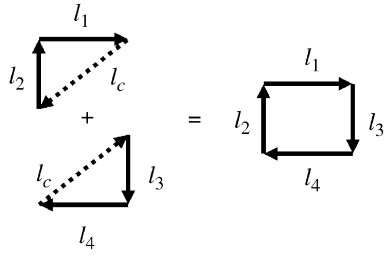

Fig. 6. Representation of a rectangular dislocation element by summation of two triangular elements. Common leg, l_c, cancels if vertex ordering is same for both triangles. This construction is used for two of the examples in discussion.

$\mathbf{p}_1 = (20, 50, 5)$, $\mathbf{p}_2 = (80, 80, 0)$, $\mathbf{p}_3 = (50, 30, 20)$ (Fig. 7). The surface displacements for strike-, dip-, and tensile-slip are shown in Figs. 7a–c. Note again the asymmetry across the strike of the dislocation plane where displacements are larger above the hanging wall than in the footwall. Contours of the second invariant of the stress tensor, $I_2 = \frac{1}{2}(\boldsymbol{\sigma} : \boldsymbol{\sigma} - \mathrm{tr}(\boldsymbol{\sigma})^2)$, on a horizontal plane cutting through the TDE at a depth of 10 km for the same three cases (Figs. 7d–f) show both the characteristic four-quadrant pattern of deformation and the common locations of the nodal surfaces emanating from the TDE edges.

As an example of the use of multiple TDEs we consider the sub-vertical Whittier fault at the eastern edge of the Los Angeles basin. Plesch et al. (2003) constrained the location of the fault surface using well logs, earthquake relocations, and high-resolution seismic reflection data and parameterized this surface using a gap free triangular mesh of 2068 elements (Fig. 8) and a six element rectangular representation. The rectangular representation of the fault surface includes six elements with a characteristic length scale of ~10 km, somewhat smaller than those typically used to study interseismic deformation at intermediate scales, but larger than those commonly used to infer coseismic slip distributions. By assuming unit strike-slip on all dislocation elements we can calculate the deformation fields exactly and determine the sensitivity to fault geometry parameterizations using triangular dislocations as a tool to calculate displacements and stresses from the triangular mesh. The surface displacement fields from both the coarse rectangular and fine triangular parameterizations are characterized by a macro-scale four-quadrant pattern of

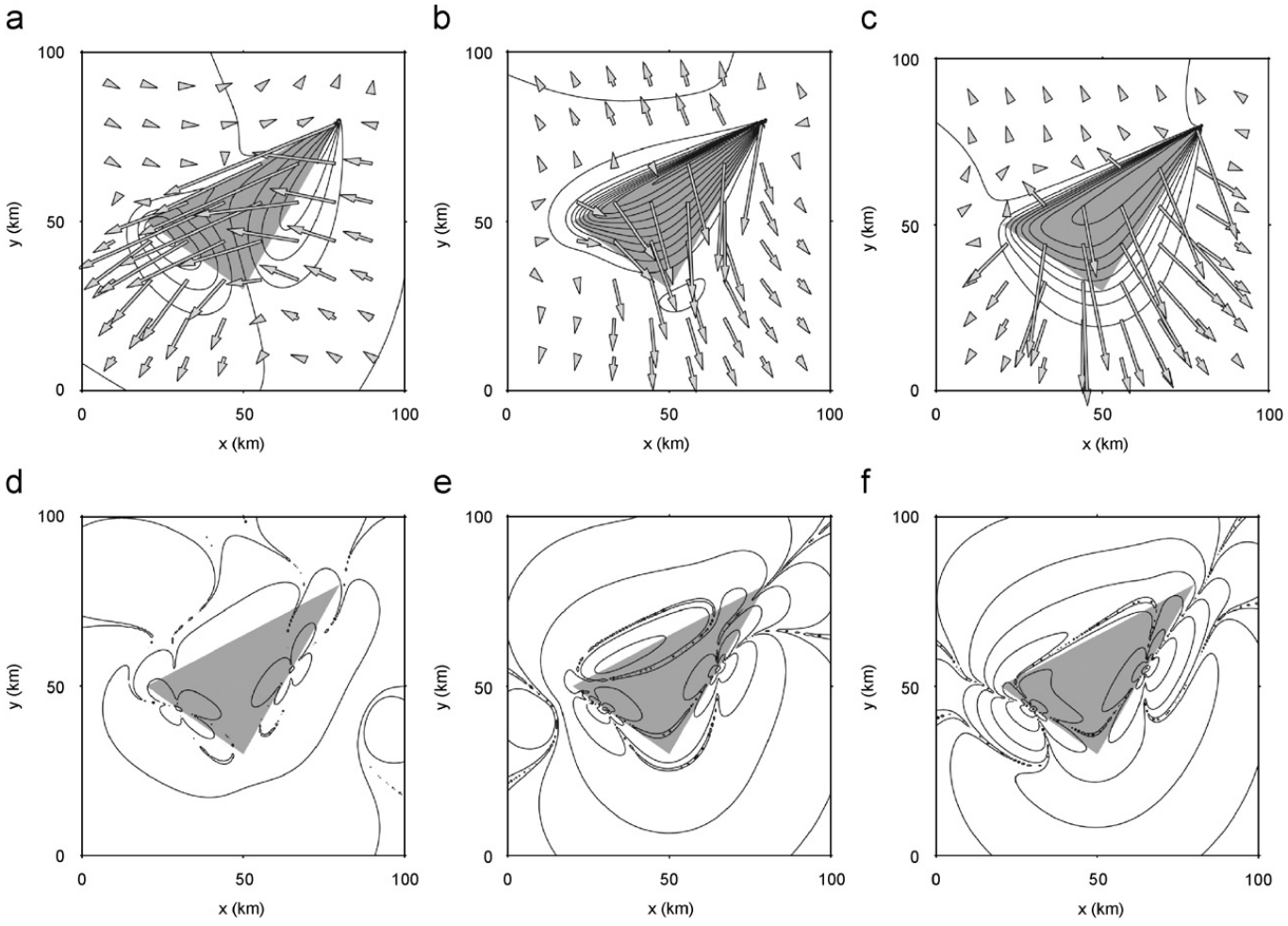

Fig. 7. Displacement and stress fields resulting from slip on an obliquely oriented, dipping, and buried triangular dislocation element. (a–c) Surface displacements for strike-, dip, and tensile-slip. Arrows give horizontal displacements and contours show vertical deformation. (d–f) Second invariant of stress tensor on a horizontal plane cutting through dislocation surface at a depth of 10 km. Note that for every case a four-quadrant pattern of deformation is observed near intersection of observation plane and triangular dislocation element.

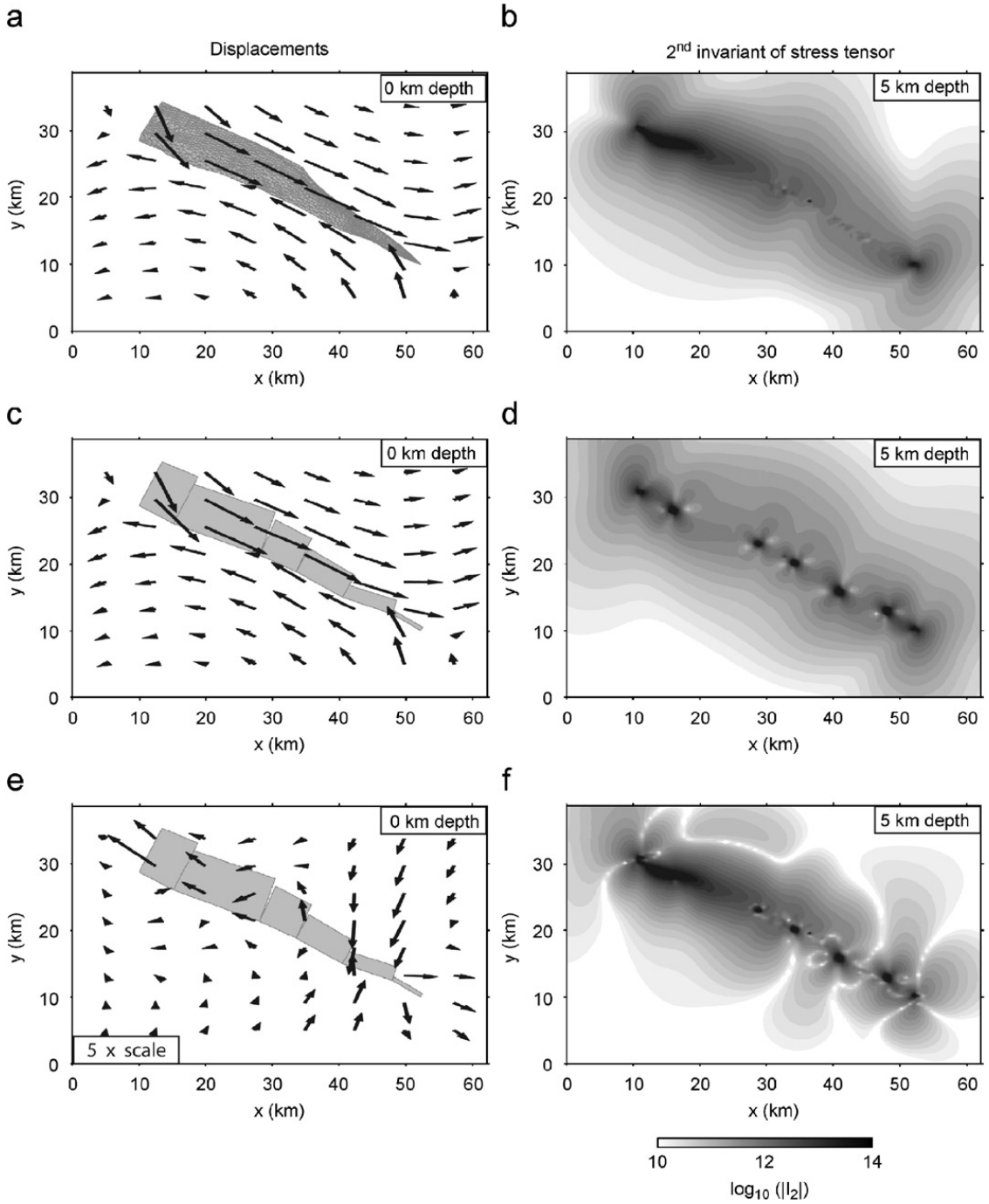

Fig. 8. Displacement and stress fields resulting from slip on different geometric representation of Whittier fault in Los Angeles Basin area of southern California. Fault dips to north at its western end and progressively steepens to southeast. (a) Black arrows are horizontal displacements from unit strike-slip motion on each of 2068 triangular elements shown in gray. (b) Horizontal displacements predicted by a model of unit strike-slip motion across each of six rectangular dislocation elements representing fault surface. (c) Residual (triangular-rectangular parameterizations) displacement field at five times scale of vectors in (a, b). Note that differential displacements are largest near hanging wall side of fault where different geometric parameterizations are closest to free surface. (c–f) Same as (a–c) only showing base 10 logarithm of absolute value of second invariant of deviatoric stress tensor on a horizontal surface cutting through fault plane at a depth of 5 km. Dark and light areas denote high and low stresses, respectively. The multiple dark regions in rectangular case are due to large stresses at gaps between rectangular dislocation elements. Note that these stress concentrations bulge outward away from fault and have effect of propagating larger stresses farther away from main fault zone than gap-free triangular representation (d). Differential stresses (f) show that largest mismatch between two parameterizations exists in hanging wall where fault surface is closest to observation coordinates.

compression and extension (Figs. 8a, b). The differential surface displacement field (Fig. 8c) highlights the residual displacements (up to ~40% at the given observation coordinates) of the calculated model displacements. These effects are largest in the hanging wall block where the fault dip is shallowest and contributions from dislocation elements at depths greater than a few kilometers contribute significantly to the predicted displacements. The differences in predicted surface displacement may be large enough to use geodetic measurements to constrain the continuity of active faults at depth.

The second invariant of the stress tensor, I_2, at depth shows significant differences between the two geometric parameterizations. Most significantly the rectangular parameterization shows the presence of high magnitude stress concentrations around each of the gaps between major segments (Figs. 8a–c). These excess stresses have the effect of adding to the overall magnitude of I_2 away from the fault zone and introducing localized stress concentrations near the fault. Thus, while a gap-free representation of fault surface may be considered more complex it may lead to a somewhat smoother stress field. Similar calculations of Coulomb failure stresses might be used to predict the locations of near-fault aftershocks.

A simple example of how rectangular approximations converge toward the exact triangular solutions can be seen by approximating a single vertical TDE with a variable number of thin, vertical, rectangular dislocation elements. We define a vertical right TDE in the x–z plane with vertices at $\mathbf{p}_1 = (40, 50, 0)$, $\mathbf{p}_2 = (60, 50, 0)$, $\mathbf{p}_3 = (60, 50, 20)$ with unit strike-slip motion and calculate the stresses along a line aligned parallel to the dipping leg but offset in the positive y direction by 1 km. The σ_{xx} components of the stress tensor for the exact triangular solution with 10 and 100 element rectangular discretizations are compared in Fig. 9. Differences between the exact and discretized approximations are minimized as the number of rectangular elements is increased, however at the coarsest 10 element discretization the stresses are, in general, lower than the exact solutions with complex behavior in between element edges. The bumps in the 10 element discretization are a result of the high stresses generated by the strain singularities at the base of the triangular approximation where the rectangular elements do not meet exactly. These comparisons demonstrate the utility of using TDEs to calculate high-resolution displacement fields rather than having to numerically integrate point sources or compute approximate rectangular discretizations.

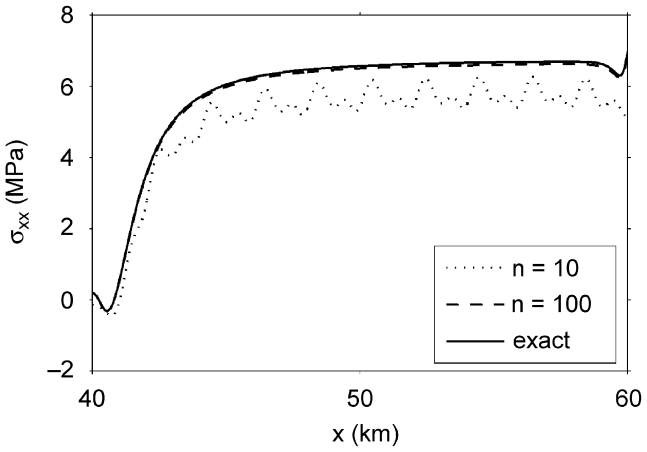

Fig. 9. Stresses from a triangular dislocation element and variable resolution rectangular approximations. Triangle lies in y–z plane with a width and depth of 20 km. Stresses are calculated along a set of observation coordinates parallel to dipping leg of a triangular dislocation element and offset in y direction by 1 km. Triangle surface is approximated using multiple rectangular dislocations whose edges match exactly except along bottom dipping leg of triangle. Stresses from rectangular approximations of triangular dislocation converge as the number of rectangular elements increases.

7. Conclusions

TDEs allow for the exact calculation of displacement strain and stress fields with gap-free representations of fault surfaces. We have detailed the algorithms necessary to carry out these calculations, including the calculation of angular dislocation slip components, accounting for the solid body displacement below the TDE, exact expressions for the strains, and defining a triangle vertex ordering scheme that enables the calculation of deformation fields from multiple TDEs in an internally consistent framework. These algorithms may find application in the analysis of geodetic data over inter-, co-, and post-seismic time scales as well is in the calculation of Coulomb failure stresses and slip evolution modeling.

Acknowledgments

Discussions with Robert Simpson and William Stuart helped to focus this work on a clear description of the algorithmic details. Reviews by David Healy and an anonymous reviewer greatly improved the writing and content of this paper.

Funding was provided by the Southern California Earthquake Center and Harvard University.

Appendix A. Supplementary material

Supplementary data associated with this article can be found in the online version at doi:10.1016/j.cageo.2006.12.003.

References

Brown, R.L., 1975. A dislocation approach to plate interaction, Ph. D. Dissertation, Massachusetts Institute of Technology, Cambridge, MA, 449pp.

Burgers, J.M., 1939. Some considerations on the fields of stress connected with dislocations in a regular crystal lattice I In: Proceedings of the Koninklijke Nederlandse Akademie Van Wetenschappen, vol. 42, pp. 293–325.

Burgmann, R., Ergintav, S., Segall, P., Hearn, E.H., McClusky, S., Reilinger, R.E., Woith, H., Zschau, J., 2002. Deformation during the 12 November 1999 Duzce, Turkey, earthquake, from GPS and InSAR data. Bulletin of the Seismological Society of America 92, 161–171.

Chinnery, M., 1961. The deformation of the ground around surface faults. Bulletin of the Seismological Society of America 51, 355–372.

Comninou, M., 1973. Angular dislocation in a half space. Ph.D. Dissertation, Northwestern University, Evanston, Ill, 45pp.

Comninou, M., Dunders, J., 1975. Angular dislocation in a half space. Journal of Elasticity 5, 203–216.

Griffith, W.A., Cooke, M.L., 2004. Mechanical validation of the three-dimensional intersection geometry between the Puente Hills blind-thrust system and the Whittier fault, Los Angeles, California. Bulletin of the Seismological Society of America 94, 493–505.

Hirth, J.P., Lothe, J., 1968. Theory of Dislocations. McGraw-Hill, New York, NY, 780pp.

Jeyakumaran, M., Rudnicki, J.W., Keer, L.M., 1992. Modeling slip zones with triangular dislocation elements. Bulletin of the Seismological Society of America 82, 2153–2169.

Maerten, F., Resor, P., Pollard, D., Maerten, L., 2005. Inverting for slip on three-dimensional fault surfaces using angular dislocations. Bulletin of the Seismological Society of America 95, 1654–1665.

Malvern, L.E., 1969. Introduction to the Mechanics of a Continuous Medium. Prentice Hall, Upper Saddle River, NJ, 713pp.

McGuire, J.J., Segall, P., 2003. Imaging of aseismic fault slip transients recorded by dense geodetic networks. Geophysical Journal International 155, 778–788.

Okada, Y., 1985. Surface deformation due to shear and tensile faults in a half-space. Bulletin of the Seismological Society of America 75, 1135–1154.

Okada, Y., 1992. Internal deformation due to shear and tensile faults in a half-space. Bulletin of the Seismological Society of America 82, 1018–1040.

Olson, E.L., Cooke, M.L., 2005. Application of three fault growth criteria to the Puente Hills thrust system, Los Angeles, California, USA. Journal of Structural Geology 27, 1765–1777.

Plesch, A., Shaw, J.H., SCEC CFM Working Group, 2003. SCEC CFM—A WWW accessible community fault model for southern California. Eos. Transactions of the American Geophysical Union, 84.

Savage, J.C., Burford, R.O., 1973. Geodetic determination of relative plate motion in central California. Journal of Geophysical Research 78, 832–845.

Thomas, A., 1993. POLY3D: A three-dimensional, polygonal element, displacement discontinuity boundary element computer program with applications to fractures, faults, and cavities in the Earth's crust. M.Sc. Thesis, Stanford University, 69pp.

Tremblay, C., 2004. Mathematics for Game Developers. Thompson, Boston, MA, 627pp.

Yoffe, E.H., 1960. The angular dislocation. Philosophical Magazine 5, 161–175.